PHOTONICS Research

Gap-surface plasmon metasurfaces for linear-polarization conversion, focusing, and beam splitting

Fei Ding,* Yiting Chen, and Sergey I. Bozhevolnyi

Centre for Nano Optics, University of Southern Denmark, Campusvej 55, DK-5230 Odense, Denmark
**Corresponding author: feid@mci.sdu.dk*

Received 26 December 2019; revised 27 February 2020; accepted 1 March 2020; posted 4 March 2020 (Doc. ID 386655); published 24 April 2020

Gap-surface plasmon (GSP) metasurfaces have attracted progressively increasing attention due to their planar configurations, ease of fabrication, and unprecedented capabilities in manipulating the reflected fields that enable integrating diverse bulk-optic-based optical components into a single ultrathin flat element. In this work, we design and experimentally demonstrate multifunctional metalenses that perform simultaneous linear-polarization conversion, focusing, and beam splitting, thereby reproducing the combined functionalities of conventional half-wave plates, parabolic reflectors, and beam splitters. The fabricated single-focal metalens incorporates properly configured distinct half-wave-plate-like GSP meta-atoms and exhibits good performance under linearly polarized incidence in terms of orthogonal linear-polarization conversion (>75%) and focusing (overall efficiency > 22%) in the wavelength spectrum ranging from 800 to 950 nm. To further extend the combined functionalities, we demonstrate a dual-focal metalens that splits and focuses a linearly polarized incident beam into two focal spots while maintaining the capability of orthogonal linear-polarization conversion. Furthermore, the power distribution between two split beams can readily be controlled by judiciously positioning the incident beam. The demonstrated multifunctional GSP-based metalenses mimic the combined functionalities of a sequence of discrete bulk optical components, thereby eliminating the need for their mutual alignment and opening new perspectives in the development of ultracompact and integrated photonic devices.

https://doi.org/10.1364/PRJ.386655

1. INTRODUCTION

In recent years, gap-surface plasmon metasurfaces (GSPMs), which consist of arrays of metallic resonant antennas, a subwavelength thin dielectric spacer, and an optically thick metal film, have attracted progressively increasing attention and provided promising solutions for cost-effective and high-performance optical devices operating in reflection due to their subwavelength-scale thickness and unprecedented control over reflected fields [1–6]. Different from conventional refractive optics that mold the flow of light through gradually accumulated phase variations during light propagation along a long distance, the gap-surface plasmon (GSP) meta-atoms comprising GSPMs can tailor the amplitude, phase, and polarization of the reflected fields directly within a subwavelength distance. As such, the resulting optical devices exhibit the advantages of low-loss, surface-confined configurations, and ease of fabrication while delivering specific functionalities with good performance and high efficiency [7–22].

In addition to the specific functionalities, strongly anisotropic GSP meta-atoms have been utilized to achieve linear-polarization-selective [23–25] or spin-selective [25,26] distinct functionalities, where each polarization state is subjected to a different wavefront transformation. However, the aforementioned linear-polarization-selective GSPMs lack the capability of polarization conversion, which is detrimental for the signal-to-noise ratio due to the overlap between the signal beam and the background. Additionally, the geometric-phase GSPMs need to be excited with circularly polarized waves that involve bulk quarter-wave plates in the optical path and therefore limit the integration potential. In this regard, multifunctional GSPMs possessing efficient linear-polarization conversion are highly desirable [27–29]. For instance, linear-polarization conversion and wavefront shaping have been demonstrated in transmission mode [27,30,31]. Furthermore, by combining a high-refractive-index silicon resonator array with a silver ground plane, the orthogonally polarized vortex beam has been experimentally realized in the telecom range [28]. Nevertheless, the performance comes at the price of a substantially thicker device and angular-sensitive operating bandwidth compared to the typical GSPMs [5].

In this work, we demonstrate multifunctional metalenses involving linear-polarization conversion, focusing, and even beam splitting by utilizing distinct half-wave-plate-like (HWP-like) GSP meta-atoms that enable efficient linear-polarization conversion along with complete phase control over reflected fields. The fabricated single-focal metalens exhibits good capability of orthogonal linear-polarization conversion (>75%) and focusing (overall efficiency > 22%) within the wavelength range of 800–950 nm. To further extend the combined functionalities, we demonstrate a dual-focal metalens that splits and focuses the x-polarized incident wave into two focused spots while maintaining the capability of orthogonal linear-polarization conversion, thereby reproducing the combined functionalities of conventional HWPs, parabolic reflectors, and power splitters. Furthermore, by changing the relative position between the incident beam and the dual-focal metalens, the power distribution between two split beams can readily be controlled.

2. RESULTS AND DISCUSSION

Figure 1(a) schematically illustrates the GSP single-focal metalens that enables linear-polarization conversion and focusing. When an x-polarized (y-polarized) plane wave is normally incident on the metalens, the reflected waves become cross-polarized, gain appropriate phase shifts, and finally form a diffraction-limited focal spot. To obtain a reflective linear-polarization-converting metalens, an array of anisotropic GSP meta-atoms are used to achieve efficient linear-polarization conversion, along with complete phase control over the reflected fields, as shown in Fig. 1(a). In this way, each GSP element functions as a nanoscale HWP (nano-HWP) capable of manipulating, simultaneously and independently, both polarizations and phases of the reflected fields. The GSP unit cell consists of a rectangular- or ellipse-shaped Au nanoantenna tilted 45° with respect to the x axis, a silicon dioxide (SiO_2) middle spacer, and a continuous Au film, which supports the typical GSP resonance due to the near-field interaction between two metallic layers and enables orthogonal linear-polarization conversion [5,32–34]. The unit cells are periodically distributed in both the x and y directions with a subwavelength periodicity of $p = 550$ nm, which can eliminate any unwanted diffraction orders. The thickness of the SiO_2 spacer layer is optimized to be $t_s = 110$ nm to ensure good performance and sufficient phase response at the design wavelength of $\lambda = 850$ nm. The thickness of the Au nanoantennas is $t_m = 80$ nm, and the bottom Au layer is thick enough ($d = 130$ nm) to block light transmission. To realize efficient nano-HWPs, we implemented three-dimensional (3D) full-wave simulations with COMSOL Multiphysics (version 5.3) to optimize the topmost Au nanoantennas. In the simulation, a unit cell was modeled in the simulation domain, where periodic boundary conditions were applied in both the x and y directions, and a perfectly matching layer (PML) was used above the structure. The SiO_2 dielectric layer is regarded as a lossless material with a constant relative permittivity of $\varepsilon = 2.1$, while the permittivity of Au is described by the Drude model fitted with the experimental data [35], where the damping rate is increased by a factor of 3 to consider the surface scattering and grain boundary effects. To excite the unit cell, an x-polarized plane wave was set to impinge normally on the structure, and both x- and y-polarized reflected components were examined in terms of the cross-polarized reflectivity R_{cr}, co-polarized reflectivity R_{co}, linear polarization-conversion ratio PCR [$PCR = R_{cr}/(R_{cr} + R_{co})$], and cross-polarized reflection phase φ_{cr}. From Fig. 1(b), it is clear that all four elements yield highly efficient linear-to-linear polarization transformation with the polarization-conversion ratio PCR exceeding 95% and the averaged cross-polarized reflectivity reaching ~85% at the design wavelength of $\lambda = 850$ nm. More importantly, we can realize a linear phase gradient with a phase increment of $\pi/2$ between adjacent meta-atoms for the cross-polarized reflected light with the four selected elements [Fig. 1(c)]. As a final comment, it is worth noting that the meta-atoms work properly within the wavelength range of 800–900 nm (Appendix A).

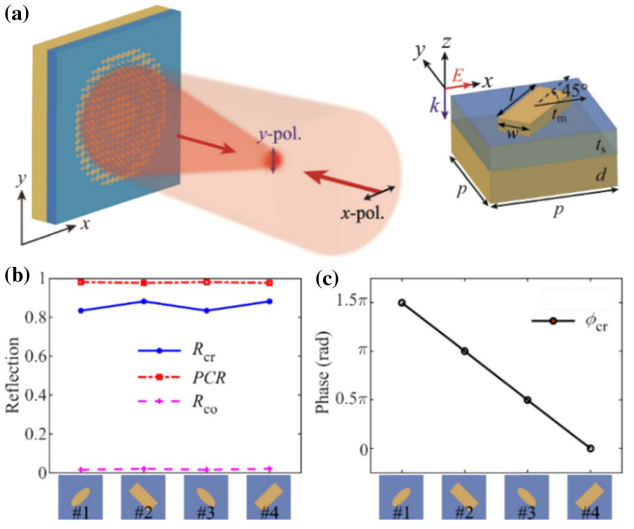

Fig. 1. Schematic of the GSP single-focal metalens for linear-polarization conversion and focusing. (a) Artistic rendering of the working principle, which converts a normally incident x-polarized beam to a y-polarized focused beam in reflection. The right panel shows the meta-atom that consists of an Au nanoantenna on top of a SiO_2 spacer and an Au substrate. (b) Simulated cross-polarized reflectivity R_{cr}, co-polarized reflectivity R_{co}, and orthogonal linear-polarization-conversion ratio PCR of the four elements at the design wavelength of $\lambda = 850$ nm. (c) Simulated cross-polarized reflection phase φ_{cr} of the four elements at the design wavelength of $\lambda = 850$ nm. The dimensions (l, w) of elements 1–4 are (228 nm, 90 nm), (155 nm, 360 nm), (90 nm, 228 nm), and (360 nm, 155 nm), respectively.

To integrate the functionalities of a bulky HWP and a parabolic reflector in a single planar device, the metalens should first incorporate the hyperbolic phase profile, which is given by $\varphi(x, y) = \frac{2\pi}{\lambda}(\sqrt{x^2 + y^2 + f_0^2} - f_0)$, where λ is the design wavelength in free space, f_0 is the focal length, and (x, y) represents the coordinates of a meta-atom within the metalens. Appendix A displays the phase profile of the designed metalens with a diameter of $D = 50$ μm and a focal length of $f_0 = 60$ μm. The phase profile is then discretized in a step of $\pi/2$ on the x-y plane and represented with proper meta-atoms (see more details in Appendix B). Within the metasurface, each

meta-atom is rotated by 45° with respect to the x axis, ensuring the orthogonal linear-polarization conversion for the x- or y-polarized incident light. The designed metalens was fabricated with the standard electron beam lithography (EBL) and thin-film deposition techniques. First, a 3-nm-thick titanium (Ti), a 130-nm-thick Au, and a 3-nm-thick Ti layer were deposited onto a double-polished silicon substrate using thermal evaporation with the deposition rates of 0.02, 0.1, and 0.02 nm/s, respectively. Then a 110-nm-thick SiO_2 spacer layer was deposited via radio frequency (RF) sputtering with the deposition rate of 0.05 nm/s. After that, a 200-nm-thick PMMA (4% in anisole, Micro Chem) layer was spin coated on the SiO_2 layer, baked at 180°C for 2 min, and exposed at an acceleration voltage of 30 keV. After exposure, the metasurface was developed in the solution of methyl isobutyl ketone (MIBK) and isopropyl alcohol (IPA) of MIBK: IPA = 1:3 for 45 s. Following development, a 3-nm-thick Ti adhesion layer and a 77-nm-thick Au layer were deposited using electron-beam evaporation. Finally, the top Au patterns were formed after a lift-off process. Figure 2(a) shows the scanning electron microscope (SEM) images of the fabricated sample with different magnifications (see the additional SEM image in Appendix C).

Following the fabrication, we characterized the prepared sample using a custom-built optical setup, which includes a couple of optical components mounted on a 3D translation stage (see more details in Appendix D). By moving all the mounted components together along the axis of light propagation (z direction) with a step of 2 μm, the intensity profiles at different x-y planes are recorded in sequence. In Fig. 2(b), we plot the measured cross-polarized intensity profiles at the design wavelength of $\lambda = 850$ nm when the metalens is illuminated with an x-polarized Gaussian beam at normal incidence. It is clearly observed that the cross-polarized reflected beam is well focused on the corresponding focal plane. Additionally, the measured intensity distributions along the x and y lines cutting through the center of the focal spot are in good agreement with the calculated profiles, which proves the diffraction-limited focusing property [Fig. 2(c)]. By stitching all the captured images together, the polarization-converted light intensity distributions on the x-z plane are achieved and displayed in Fig. 2(d), revealing the revolution of the focusing phenomena. The measured focal length is about 62 μm, close to the designed value of $f_0 = 60$ μm. Besides the fabrication errors, here the discrepancy mainly originates from the limited resolution (1 μm) and hysteresis errors in the translation stage positioning. Importantly, the fabricated single-focal metalens shows good performance at other wavelengths, verifying the broadband characteristic (see more details in Appendix E).

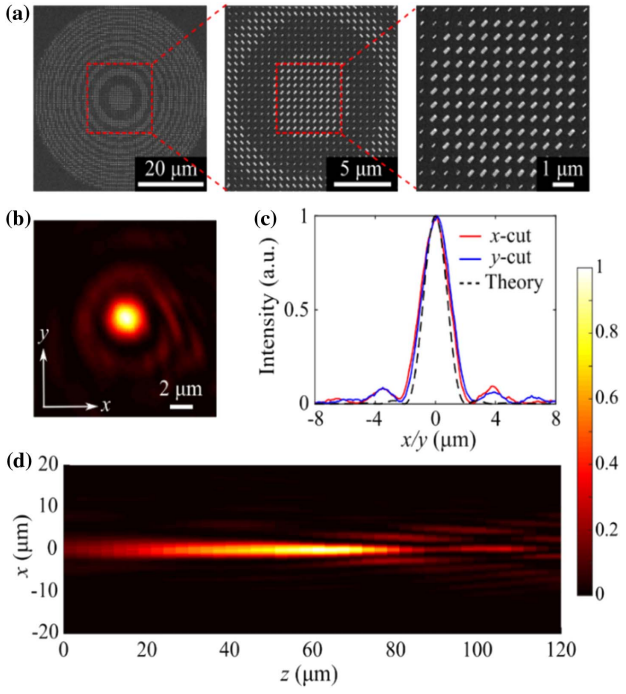

Fig. 2. Experimental demonstration of the GSP single-focal metalens for linear-polarization conversion and focusing. (a) Top-view SEM images of the fabricated sample with different magnifications. (b) Measured focal spot profiles in cross-polarization. (c) Measured intensity distributions in cross-polarization along the horizontal (x) and vertical (y) line cutting through the center of the focal spot in comparison with diffraction-limited focal spot profile. (d) Measured intensity profiles of the reflected beam in the x-z plane in cross-polarization. The x-polarized Gaussian beam is normally incident on the central part of the sample at the design wavelength of $\lambda = 850$ nm.

Besides the good focusing characteristics, this single-focal metalens features excellent capability of linear-polarization conversion. At the design wavelength of $\lambda = 850$ nm, the measured PCR is found to be ~86%. Remarkably, the good linear-polarization-conversion performance is maintained over a wide spectrum ranging from 800 to 950 nm, indicating the broadband response with good focusing characteristics and highly efficient orthogonal linear-polarization conversion (Fig. 3). When the working wavelength moves to a short wavelength that deviates further from the design value, for instance, $\lambda = 775$ nm, the linear-polarization conversion becomes deteriorated with the PCR reaching only ~31%, which can likely be ascribed to the large variations in cross-polarized reflection amplitudes produced by different elements constructing the metalens. Although the single-focal metalens shows

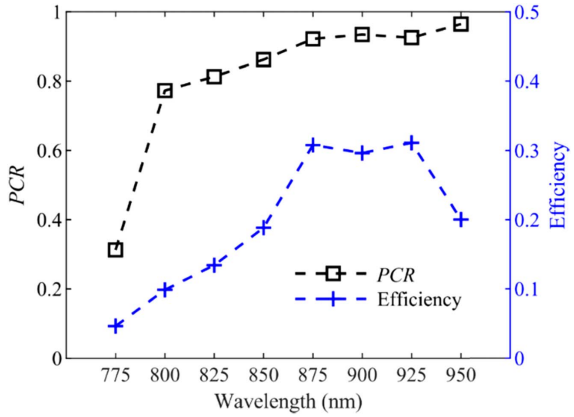

Fig. 3. Measured PCR and absolute efficiencies at the corresponding focal plane as functions of wavelength. The PCR and absolute efficiency were integrated and averaged over two measured intensity profiles with the relative error being within 3%.

poor capability of orthogonal linear-polarization conversion at $\lambda = 775$ nm, the focusing quality remains high, and the cross-polarized light still assembles a tiny focal spot (Appendix E).

To further study the operating performance of the fabricated metalens, the absolute focusing efficiency, defined as the ratio of the light intensity from the focal spot to the incident intensity, is measured and calculated at the investigated wavelength spectrum as shown in Fig. 3. As expected, the polarization-converted beam is dominating in the corresponding focal spots within the wavelength range of 800–950 nm, where an averaged focusing efficiency of ~22% has been obtained, consistent with the reported value of a near-infrared GSP focusing mirror [16]. The maximum focusing efficiency (~31%) was achieved at $\lambda = 875$ nm, which is deviated from the designed value. We believe the aforementioned discrepancies are mainly ascribed to the imperfections of the fabricated nanoantennas, the increased damping caused by the Ti adhesion layer, and different excitation conditions in the simulation and experiment. The efficiency could be increased with hybrid GSP resonators composed of high-index dielectric antennas on top of the dielectric-coated metallic substrate. As a final comment, it should be emphasized that the single-focal metalens shows identical properties in orthogonal linear-polarization conversion and beam focusing when the incident light is changed to y polarization, in accordance with the symmetry of the meta-atoms comprising the metasurface (see more details in Appendix F). If the metalens is illuminated with a circularly polarized (CP) beam, then a CP focused spot with the same helicity will be formed.

In addition to linear-polarization conversion and focusing, it is possible to extend the functionalities of our design. Because beam splitters are indispensable in a variety of optical systems [36], we herein propose a dual-focal metalens that splits and focuses a linearly polarized incident wave into two slightly focused spots while maintaining the capability of orthogonal linear-polarization conversion [Fig. 4(a)], thereby mimicing the combined functionalities of conventional HWPs, parabolic reflectors, and beam splitters. In this way, such a dual-focal metalens serves as a viable ultra-thin substitute for these three bulky optical components. In our design, the dual-focal metalens uses the segmented configuration composed of two submetalenses, where each submetalens can focus the linearly polarized incident beam into an orthogonally polarized beam at the same focal plane (see more details in Appendix G). Therefore, the incident power is split and confined in each focal spot. Figure 4(b) presents the SEM images of the fabricated dual-focal metalens, where the focal length is set to be $f = 60$ μm and the two foci are well separated with a distance of $s = 20$ μm at the design wavelength of $\lambda = 850$ nm. Following the fabrication, we used the same setup to characterize the dual-focal metalens sample and plotted the cross-polarized intensity profiles at the corresponding focal plane in Fig. 4(c). As predicted, two diffraction-limited focal spots are formed at different locations in the same focal plane when an x-polarized Gaussian beam is incident on the central part of the sample at $\lambda = 850$ nm. However, due to the imperfections in fabrication and misalignment of the optical setup, the two focal spots show non-identical power distributions, and thus the power split ratio slightly deviates from 50:50 [Fig. 4(d)]. To

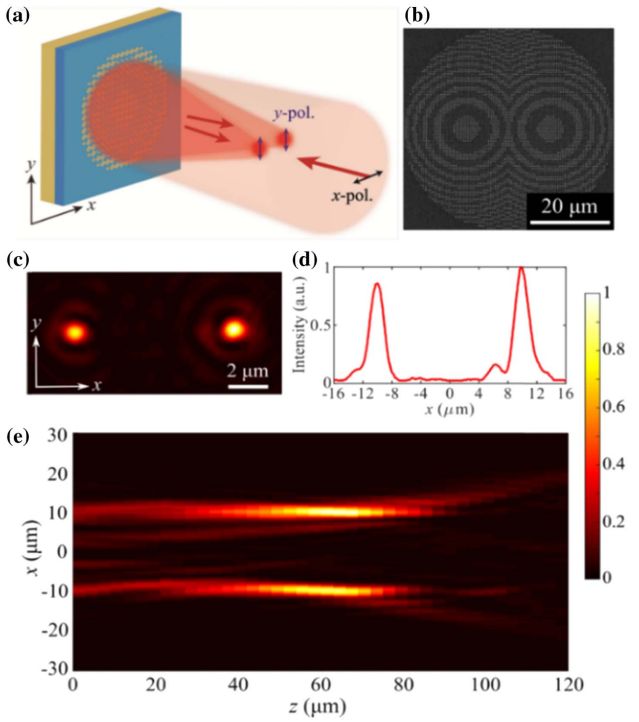

Fig. 4. Design, fabrication, and optical characterization of the dual-focal metalens for linear-polarization conversion, focusing, and beam splitting. (a) Schematic of the dual-focal metalens that converts a normally incident x-polarized beam into two y-polarized focused spots in reflection. (b) Top-view SEM image of the fabricated dual-focal sample. (c) Measured focal spot profiles in cross-polarization. (d) Measured intensity distributions in cross-polarization along the horizontal (x) line cutting through the centers of the focal spots. (e) Measured intensity profiles of the reflected beam in the x-z plane in cross-polarization. The x-polarized Gaussian beam is normally incident on the central part of the sample at the design wavelength of $\lambda = 850$ nm.

verify the focusing capability, we measure the beam intensity profiles in the x-z cross-section within a 120 μm span near the focal spots, where an orthogonally aligned linear analyzer was placed in front of the camera to collect the cross-polarized signal. As shown in Fig. 4(e), the polarization-converted reflected waves were slightly focused after propagating over a certain distance. The measured focal lengths of the two foci are found to be ≈62 and 60 μm, respectively, which are close to the designed value. Here, it should be mentioned that the intrinsic crosstalk between two sublenses in such a segmented configuration deteriorates the focusing performance to some extent. For example, compared with the single-focal metalens, the background has been increased and the focal spots along the x axis have been elongated due to the crosstalk and reduced aperture of the individual submetalens along the x direction. Even though there is perturbation, the dual-focal metalens exhibits reasonable performance in terms of linear-polarization conversion, focusing, and beam splitting.

In practical applications, it is highly desirable to achieve various split ratios, which is essentially related to controlling the relative intensities from two focal spots. We realize this by changing the distance between the sample and the incident Gaussian beam along the x direction as shown in Fig. 5(a).

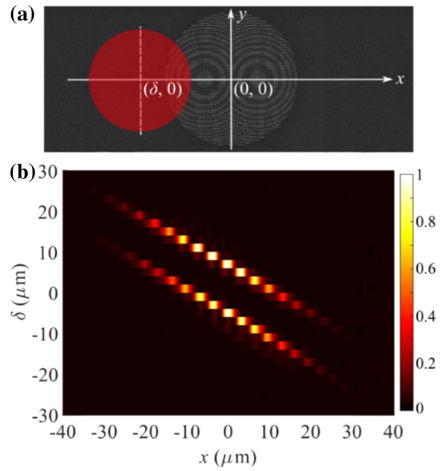

Fig. 5. Generation of switchable power distributions with different distances between the incident beam and the dual-focal metalens. (a) Schematic diagram of the distance between the incident beam and the dual-focal metalens. (b) Measured power distributions with different distances between the incident beam and the dual-focal metalens.

Figure 5(b) shows the continuous generation of switchable power distributions along the x direction in the corresponding focal plane when the incident light is gradually moved from the left to the right with a step of 2 μm. A gradual monotonic transition between the two focal spots is evident, where the intensities of the two foci can be tuned by positioning the incident beam. If the incident beam is impinging on the left and right submetalenses equally ($\delta = 0$), two focal spots with nearly identical intensities are formed in the focal plane. Once the beam is moved away from the center of the sample ($-10\ \mu\text{m} \le \delta \le 10\ \mu\text{m}$), one of the focal spots becomes brighter while the other is getting weaker. However, when the incident beam moves further away from the sample ($\delta < -10\ \mu\text{m}$ or $\delta > 10\ \mu\text{m}$), both spots become weaker and finally disappear due to the weak interaction between the light and the metalens.

3. CONCLUSIONS

In this work, we have utilized distinct HWP-like GSP meta-atoms to realize multifunctional metalenses that produce the combined functionalities of conventional HWPs, parabolic reflectors, and even beam splitters. The fabricated single-focal metalens exhibits good capability of orthogonal linear-polarization conversion (>75%) and focusing (overall efficiency > 22%) within the wavelength range of 800–950 nm under linearly polarized excitation. Capitalizing on this design, we extended the combined functionalities and demonstrated a dual-focal metalens that splits and focuses a linearly polarized incident wave into two focused spots while maintaining the capability of orthogonal linear-polarization conversion. The demonstrated multifunctional GSP-based metalenses mimic the combined functionalities of a sequence of discrete bulk optical components, thereby eliminating the need for their mutual alignment, and facilitate the development of ultracompact and integrated photonic devices due to the compact footprint, integration compatibility, and remarkable performance.

APPENDIX A: RESPONSE OF THE META-ATOMS AS A FUNCTION OF WAVELENGTH

Figure 6 shows the performance of selected elements as functions of wavelength, validating the broadband property.

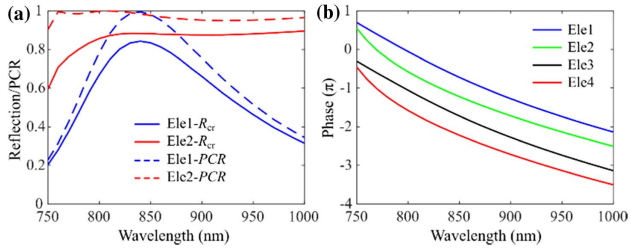

Fig. 6. (a) Simulated cross-polarized reflectivity R_{cr} and orthogonal linear-polarization-conversion ratio PCR for elements 1 and 2. (c) Simulated cross-polarized reflection phase φ_{cr} for elements 1–4 that provide a linear phase variation spanning a 2π range.

APPENDIX B: SCHEMATIC AND DESIGN OF THE SINGLE-FOCAL METALENS

Figure 7(a) shows the calculated phase profile of the designed single-focal metalens at $\lambda = 850$ nm. The phase is then discretized and represented with the selected elements [Fig. 7(b)].

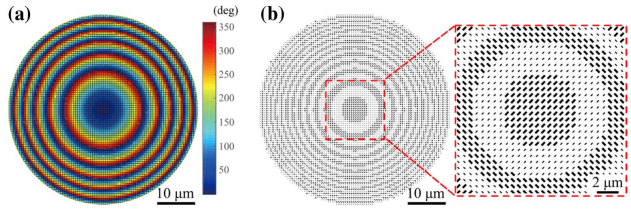

Fig. 7. (a) Calculated phase profile and (b) designed geometry of the single-focal metalens with the diameter of $D = 50$ μm and the focal length of $f = 60$ μm at the wavelength of $\lambda = 850$ nm.

APPENDIX C: ADDITIONAL SEM IMAGE OF THE FABRICATED SINGLE-FOCAL METALENS

Figure 8 shows the zoomed SEM image of the fabricated single-focal lens, where the cross- and brick-shaped elements can be clearly observed.

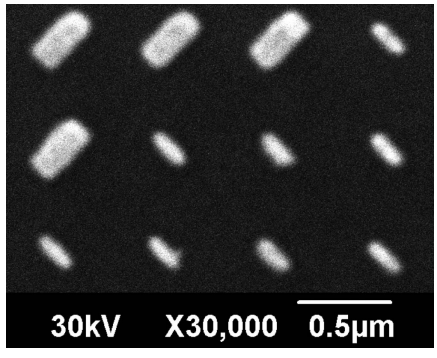

Fig. 8. Additional SEM image of the fabricated single-focal metalens, which shows meta-atoms with different shapes more clearly.

APPENDIX D: SETUP FOR CHARACTERIZATION

The performance of the metalens was studied using a custom-built optical system as shown in Fig. 9. The collimated optical beam from a continuous-wave tunable Ti:sapphire laser (Spectra-Physics) passes through an HWP (Thorlabs, AHWP05M-980) and two linear polarizers (Thorlabs, LPVIS100-MP2) to create pure linearly polarized light with controlled intensity. Then a long-working-distance objective (Mitutoyo, 5× magnification, NA = 0.14) is used to slightly focus the linearly polarized light onto the metalens through a beam splitter (Thorlabs, BS011) to get a beam spot smaller than the metalens. In order to capture the focused images at different x-y planes, a microscope imaging system including a long-working-distance objective (Mitutoyo, 50× magnification, NA = 0.55), a tube lens with a focal length of $f = 100$ mm (Thorlabs, AC254-100-B-ML), a linear polarizer (Thorlabs, LPVIS100-MP2), and a CCD camera (Mightex) is mounted together on a 3D translation stage (black dashed frame). During the measurement, the 3D stage is first moved to image the surface of the metalens. After that, the mounted microscope imaging system is moved along the z direction to record the images at different x-y planes. Subsequently, the intensity distribution along the z direction can be obtained by stitching all the captured images.

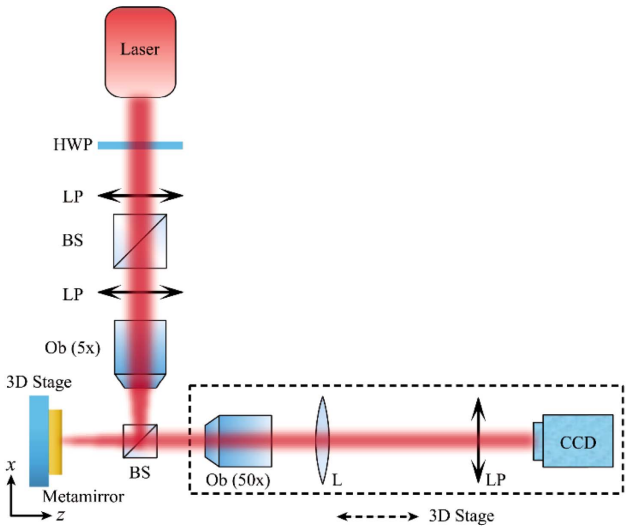

Fig. 9. Schematic of the experimental setup for characterizing the metalens. HWP, half-wave plate; LP, linear polarizer; BS, beam splitter; Ob, objective; L, lens.

APPENDIX E: CHARACTERIZATION OF THE SINGLE-FOCAL METALENS AT OTHER WAVELENGTHS

Figure 10 displays the experimental results at other wavelengths, indicating the broadband performance.

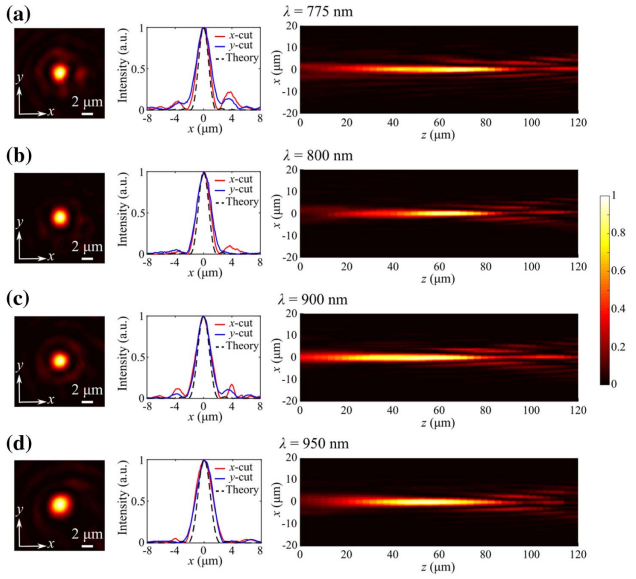

Fig. 10. Measured intensity profiles of the single-focal metalens at wavelengths of (a) 775 nm, (b) 800 nm, (c) 900 nm, and (d) 950 nm. All the intensity profiles are measured in cross-polarization, and the incident light is a normally incident x-polarized Gaussian beam.

APPENDIX F: MEASURED INTENSITY PROFILES OF THE SINGLE-FOCAL METALENS UNDER *Y*-POLARIZED EXCITATION AT 850 NM WAVELENGTH

As expected, the fabricated single-focal lens also works pretty well under y-polarized incidence (Fig. 11).

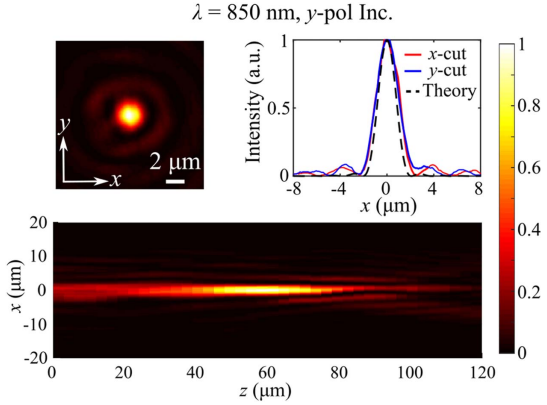

Fig. 11. Optical characterization of the single-focal metalens at the wavelength of 850 nm when a y-polarized Gaussian beam is normally incident on the metalens. All the intensity profiles are measured in cross-polarization.

APPENDIX G: SCHEMATIC AND DESIGN OF THE DUAL-FOCAL METALENS

The phase profile and designed geometry of the dual-focal lens are shown in Fig. 12.

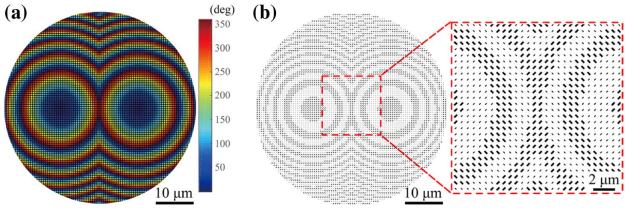

Fig. 12. (a) Calculated phase profile and (b) designed geometry of the dual-focal metalens with the diameter of $D = 50$ μm, the focal length of $f_0 = 60$ μm, and the separation of $s = 20$ μm at the wavelength of $\lambda = 850$ nm. The phase is calculated with $\varphi(x,y) = \begin{cases} \frac{2\pi}{\lambda}\left[\sqrt{(x+\frac{s}{2})^2+y^2+f_0^2}-\sqrt{(\frac{s}{2})^2+f_0^2}\right] & (x \ll 0) \\ \frac{2\pi}{\lambda}\left[\sqrt{(x-\frac{s}{2})^2+y^2+f_0^2}-\sqrt{(\frac{s}{2})^2+f_0^2}\right] & (x > 0) \end{cases}$.

Funding. FP7 Ideas: European Research Council (341054); Villum Fonden (00022988, Award in Technical and Natural Sciences 2019); Syddansk Universitet (SDU2020).

Disclosures. The authors declare no conflicts of interest.

REFERENCES

1. N. Yu and F. Capasso, "Flat optics with designer metasurfaces," Nat. Mater. **13**, 139–150 (2014).
2. H. T. Chen, A. J. Taylor, and N. Yu, "A review of metasurfaces: physics and applications," Rep. Prog. Phys. **79**, 076401 (2016).
3. H. H. Hsiao, C. H. Chu, and D. P. Tsai, "Fundamentals and applications of metasurfaces," Small Methods **1**, 1600064 (2017).
4. F. Ding, A. Pors, and S. I. Bozhevolnyi, "Gradient metasurfaces: a review of fundamentals and applications," Rep. Prog. Phys. **81**, 026401 (2018).
5. F. Ding, Y. Yang, R. Deshpande, and S. I. Bozhevolnyi, "Review of gap-surface plasmon metasurfaces: fundamentals and applications," Nanophotonics **7**, 1129–1156 (2018).
6. S. Sun, Q. He, J. Hao, S. Xiao, and L. Zhou, "Electromagnetic metasurfaces: physics and applications," Adv. Opt. Photonics **11**, 380–479 (2019).
7. S. Sun, K.-Y. Yang, C.-M. Wang, T.-K. Juan, W. T. Chen, C. Y. Liao, Q. He, S. Xiao, W.-T. Kung, G.-Y. Guo, L. Zhou, and D. P. Tsai, "High-efficiency broadband anomalous reflection by gradient metasurfaces," Nano Lett. **12**, 6223–6229 (2012).
8. Q. Yang, X. Chen, Q. Xu, C. Tian, Y. Xu, L. Cong, X. Zhang, Y. Li, C. Zhang, X. Zhang, J. Han, and W. Zhang, "Broadband terahertz rotator with an all-dielectric metasurface," Photon. Res. **6**, 1056–1061 (2018).
9. H. X. Xu, S. Ma, X. Ling, X. K. Zhang, S. Tang, T. Cai, S. Sun, Q. He, and L. Zhou, "Deterministic approach to achieve broadband polarization-independent diffusive scatterings based on metasurfaces," ACS Photon. **5**, 1691–1702 (2018).
10. W. G. Liu, B. Hu, Z. D. Huang, H. Y. Guan, H. T. Li, X. K. Wang, Y. Zhang, H. X. Yin, X. L. Xiong, J. Liu, and Y. T. Wang, "Graphene-enabled electrically controlled terahertz meta-lens," Photon. Res. **6**, 703–708 (2018).
11. A. Kristensen, J. K. W. W. Yang, S. I. Bozhevolnyi, S. Link, P. Nordlander, N. J. Halas, and N. A. Mortensen, "Plasmonic color generation," Nat. Rev. Mater. **2**, 16088 (2016).
12. S. Sun, Q. He, S. Xiao, Q. Xu, X. Li, and L. Zhou, "Gradient-index meta-surfaces as a bridge linking propagating waves and surface waves," Nat. Mater. **11**, 426–431 (2012).
13. A. Pors, M. G. Nielsen, T. Bernardin, J.-C. Weeber, and S. I. Bozhevolnyi, "Efficient unidirectional polarization-controlled excitation of surface plasmon polaritons," Light Sci. Appl. **3**, e197 (2014).
14. G. Zheng, H. Mühlenbernd, M. Kenney, G. Li, T. Zentgraf, and S. Zhang, "Metasurface holograms reaching 80% efficiency," Nat. Nanotechnol. **10**, 308–312 (2015).
15. F. Ding, J. Dai, Y. Chen, J. Zhu, Y. Jin, and S. I. Bozhevolnyi, "Broadband near-infrared metamaterial absorbers utilizing highly lossy metals," Sci. Rep. **6**, 39445 (2016).
16. A. Pors, M. G. Nielsen, R. L. Eriksen, and S. I. Bozhevolnyi, "Broadband focusing flat mirrors based on plasmonic gradient metasurfaces," Nano Lett. **13**, 829–834 (2013).
17. S. Zhang, M.-H. Kim, F. Aieta, A. She, T. Mansuripur, I. Gabay, M. Khorasaninejad, D. Rousso, X. Wang, M. Troccoli, N. Yu, and F. Capasso, "High efficiency near diffraction-limited mid-infrared flat lenses based on metasurface reflectarrays," Opt. Express **24**, 18024–18034 (2016).
18. S. Wang, P. C. Wu, V.-C. Su, Y.-C. Lai, C. Hung Chu, J.-W. Chen, S.-H. Lu, J. Chen, B. Xu, C.-H. Kuan, T. Li, S. Zhu, and D. P. Tsai, "Broadband achromatic optical metasurface devices," Nat. Commun. **8**, 187 (2017).
19. E. Maguid, I. Yulevich, D. Veksler, V. Kleiner, M. L. Brongersma, and E. Hasman, "Photonic spin-controlled multifunctional shared-aperture antenna array," Science **352**, 1202–1206 (2016).
20. F. Ding, A. Pors, Y. Chen, V. A. Zenin, and S. I. Bozhevolnyi, "Beam-size-invariant spectropolarimeters using gap-plasmon metasurfaces," ACS Photon. **4**, 943–949 (2017).
21. F. Ding, Y. Chen, and S. I. Bozhevolnyi, "Metasurface-based polarimeters," Appl. Sci. **8**, 594 (2018).
22. J. T. Heiden, F. Ding, J. Linnet, Y. Yang, J. Beermann, and S. I. Bozhevolnyi, "Gap-surface plasmon metasurfaces for broadband circular-to-linear polarization conversion and vector vortex beam generation," Adv. Opt. Mater. **7**, 1801414 (2019).
23. T. Cai, S. W. Tang, G. M. Wang, H. X. Xu, S. L. Sun, Q. He, and L. Zhou, "High-performance bifunctional metasurfaces in transmission and reflection geometries," Adv. Opt. Mater. **5**, 1600506 (2017).
24. F. Ding, R. Deshpande, and S. I. Bozhevolnyi, "Bifunctional gap-plasmon metasurfaces for visible light: polarization-controlled unidirectional surface plasmon excitation and beam steering at normal incidence," Light Sci. Appl. **7**, 17178 (2018).
25. S. Tang, T. Cai, H. Xu, Q. He, S. Sun, and L. Zhou, "Multifunctional metasurfaces based on the 'merging' concepts and anisotropic single-structure meta-atoms," Appl. Sci. **8**, 555 (2018).
26. M. Li, L. Jing, X. Lin, S. Xu, L. Shen, B. Zheng, Z. Wang, and H. Chen, "Angular-adaptive spin-locked retroreflector based on reconfigurable magnetic metagrating," Adv. Opt. Mater. **7**, 1900151 (2019).
27. N. K. Grady, J. E. Heyes, D. R. Chowdhury, Y. Zeng, M. T. Reiten, A. K. Azad, A. J. Taylor, D. A. R. Dalvit, and H.-T. Chen, "Terahertz metamaterials for linear polarization conversion and anomalous refraction," Science **340**, 1304–1307 (2013).
28. Y. Yang, W. Wang, P. Moitra, I. I. Kravchenko, D. P. Briggs, and J. Valentine, "Dielectric meta-reflectarray for broadband linear polarization conversion and optical vortex generation," Nano Lett. **14**, 1394–1399 (2014).
29. F. Ding, Z. Wang, S. He, V. M. Shalaev, and A. V. Kildishev, "Broadband high-efficiency half-wave plate: a supercell-based plasmonic metasurface approach," ACS Nano **9**, 4111–4119 (2015).
30. C. Zhang, C. Pfeiffer, T. Jang, V. Ray, M. Junda, P. Uprety, N. Podraza, A. Grbic, and L. Guo, "Breaking Malus' law: highly efficient, broadband, and angular robust asymmetric light transmitting metasurface," Laser Photon. Rev. **10**, 791–798 (2016).
31. S. Gao, C. S. Park, S. S. Lee, and D. Y. Choi, "All-dielectric metasurface for simultaneously realizing polarization rotation and wavefront shaping for visible light," Nanoscale **11**, 4083–4090 (2019).
32. J. Hao, Y. Yuan, L. Ran, T. Jiang, J. A. Kong, C. T. Chan, and L. Zhou, "Manipulating electromagnetic wave polarizations by anisotropic metamaterials," Phys. Rev. Lett. **99**, 063908 (2007).

33. J. Hao, Q. Ren, Z. An, X. Huang, Z. Chen, M. Qiu, and L. Zhou, "Optical metamaterial for polarization control," Phys. Rev. A **80**, 023807 (2009).
34. C. Qu, S. Ma, J. Hao, M. Qiu, X. Li, S. Xiao, Z. Miao, N. Dai, Q. He, S. Sun, and L. Zhou, "Tailor the functionalities of metasurfaces based on a complete phase diagram," Phys. Rev. Lett. **115**, 235503 (2015).
35. P. B. Johnson and R. W. Christy, "Optical constants of the noble metals," Phys. Rev. B **6**, 4370–4379 (1972).
36. X. Zhang, R. Deng, F. Yang, C. Jiang, S. Xu, and M. Li, "Metasurface-based ultrathin beam splitter with variable split angle and power distribution," ACS Photon. **5**, 2997–3002 (2018).